










Cite this: *J. Mater. Chem. A*, 2024, 12, 7631

# Optimisation of the electrochemical performance of $(\text{Nd,Gd})_{1/3}\text{Sr}_{2/3}\text{CoO}_{3-\delta}$ cathode for solid oxide fuel cells via spray-pyrolysis deposition and decoration with Ag nanoparticles†

Paula Rosendo Santos, <sup>a</sup> Domingo Pérez-Coll, <sup>b</sup> M. Teresa Azcondo, <sup>a</sup> Glenn C. Mather, <sup>b</sup> Álvaro Muñoz-Noval, <sup>cd</sup> Eduardo Salas-Colera, <sup>ce</sup> Ulises Amador, <sup>a</sup> Khalid Boulahya <sup>f</sup> and Daniel Muñoz-Gil <sup>\*bf</sup>

Single-step synthesis and deposition of composite solid oxide fuel cell cathodes of composition  $(\text{Nd,Gd})_{1/3}\text{Sr}_{2/3}\text{CoO}_{3-\delta} : \text{Ce}_{0.9}(\text{Gd,Nd})_{0.1}\text{O}_{1.95}$  (70 : 30 w : w) with and without the addition of Ag nanoparticles (Ag NPs) was achieved employing spray pyrolysis and low-temperature sintering at 900 °C. Spray-pyrolysis-prepared materials offered improved microstructure with smaller particle size and higher porosity (extended triple phase boundary) in comparison to slurry-coated electrodes of analogous composition. Impedance spectroscopy of symmetrical cells of the composite air electrodes indicated a lower resistive response of the spray-pyrolysis-prepared electrodes with lower overall polarisation resistance ( $R_p$ ), attributable to improved oxygen surface exchange and oxide-ion diffusion processes. Further reduction in  $R_p$  was achieved on decoration of the composite air electrodes with Ag NPs; the decorated composites were characterised by high resolution transmission electron microscopy (HRTEM) and high-angle annular dark-field scanning transmission electron microscopy (HAADF-STEM). Ag K-edge X-ray Absorption Near Edge Structure (XANES) and Extended X-ray Absorption Fine Structure (EXAFS) of  $\text{Ce}_{0.9}\text{Gd}_{0.1}\text{O}_{2-\delta}:\text{Ag}$  spray-pyrolysed composites indicated that the Ag nanoparticles exhibit a core-shell structure with a  $\text{Ag}_2\text{O}$  outer layer calculated to be two unit cells in thickness. The outer particle shell is suggested to participate in the enhanced electrochemical response, lowering the electrode polarisation response of symmetrical cells below 700 °C. Anode-supported single-cell fuel cells corresponding to the composite air electrode with Ag NPs and a thin YSZ-CGO electrolyte provided a maximum power density of 0.6 W cm<sup>-2</sup> at 700 °C.

Received 28th September 2023  
Accepted 15th February 2024

DOI: 10.1039/d3ta05917k

rsc.li/materials-a

## 1. Introduction

Hydrogen will play a crucial role as a vector in the strategy to implement a sustainable energy model given its low environmental impact and potential abundance. Solid oxide fuel cells (SOFCs) are one of the key technologies that could enable the development of a hydrogen economy since they efficiently and

reliably convert hydrogen to electricity. The high operating temperature of SOFCs (700–1000 °C) proffers kinetics benefits but should ideally be reduced to the intermediate temperature (IT) range (400–650 °C) to facilitate commercialisation through minimising manufacturing costs, prolonging device life, and expanding the field of application. Nevertheless, the decrease in operation temperature increases polarisation resistance and reduces cell performance. To minimise polarisation losses, the design, synthesis and processing of materials are required to achieve a competitive SOFC performance in the IT range.<sup>1</sup>

The cathode polarisation resistance is the main potential loss on reducing the operating temperature due to the relatively high activation energy associated with the oxygen reduction reaction (ORR).<sup>1</sup> Considerable research efforts are, therefore, focused on improving SOFC cathode materials for intermediate-temperature applications. The ORR involves various physicochemical processes of electro-active oxygen species (diffusion of oxygen gas, adsorption, dissociation, reduction, surface and bulk diffusion and charge transfer).<sup>2,3</sup> The ORR is highly dependent on the composition and micro-structural characteristics of the cathode, including porosity, surface

<sup>a</sup>Universidad San Pablo-CEU, CEU Universities, Facultad de Farmacia, Departamento de Química y Bioquímica, Urbanización Montepríncipe, Boadilla del Monte, 28668, Madrid, Spain. E-mail: [dmunozgi@ucm.es](mailto:dmunozgi@ucm.es)

<sup>b</sup>Instituto de Cerámica y Vidrio (ICV), CSIC, C/Kelsen, 5, 28049 Madrid, Spain

<sup>c</sup>Spline Spanish CRG Beamline, ESRF, 6 Rue J. Horowitz, Isere/Rhone-Alpes, Grenoble, 38042, France

<sup>d</sup>Departamento de Física de Materiales, Facultad de Físicas, Universidad Complutense Madrid, 28040, Madrid, Spain

<sup>e</sup>Instituto de Ciencia de Materiales de Madrid (ICMM), CSIC, Sor Juana Inés de la Cruz, 3, 28049, Madrid, Spain

<sup>f</sup>Departamento de Química Inorgánica I, Facultad de Ciencias Químicas, Universidad Complutense, 28040, Madrid, Spain

† Electronic supplementary information (ESI) available. See DOI: <https://doi.org/10.1039/d3ta05917k>



area and grain size.<sup>4</sup> The lowest area-specific resistance (ASR) values are generally observed for nanosized materials with a large surface area, requiring optimisation of synthesis and processing.<sup>5</sup>

One method demonstrated to offer tailored microstructures is spray pyrolysis, which deposits thin films with controlled thickness and uniformity through atomisation of a precursor solution producing a film on contact with a heated substrate (250–500 °C). SP has been used to deposit various cathode materials for SOFCs, such as  $\text{La}_{0.84}\text{Sr}_{0.16}\text{MnO}_{3-\delta}$ ,<sup>6</sup>  $\text{La}_{0.6}\text{Sr}_{0.4}\text{Co}_{0.2}\text{Fe}_{0.8}\text{O}_{3-\delta}$ <sup>7</sup> and  $\text{La}_{0.6}\text{Sr}_{0.4}\text{Co}_{0.2}\text{Fe}_{0.8}\text{O}_{3-\delta}:\text{Ce}_{0.9}\text{Gd}_{0.1}\text{O}_{2-\delta}$  composites.<sup>8</sup> V. Zapata-Ramírez *et al.* reported the synthesis of  $\text{SrFeO}_{3-\delta}$ -based cathodes deposited by spray pyrolysis with enhanced electrode behaviour due to improved homogeneity, distribution, and adhesion at the electrode–electrolyte interface.<sup>9</sup> Moreover, the methodology resulted particularly successful for the deposition of active interlayers to improve the electrochemical performance.<sup>10,11</sup>

The use of silver nanoparticles (Ag NPs) in SOFC cathode materials is attractive due to their high catalytic activity and stability, which can improve the performance and durability of the cell.<sup>12–14</sup> Ag NPs promote the ORR, producing a higher power density and lower polarisation resistance, and may also arrest degradation. The formation of Ag nanoparticles on the cathode surface has been achieved on doping the cathode composition with Ag then exsolving on treatment in a reducing atmosphere, as is the case for Ag-doped  $\text{La}_{0.85-x}\text{Sr}_{0.15}\text{Ag}_x\text{FeO}_{3-\delta}$  prepared by a wet-synthesis route<sup>12</sup> or  $\text{Ba}_{1-x}\text{Ag}_x\text{Co}_{0.7}\text{Fe}_{0.2}\text{Nb}_{0.1}\text{O}_{3-\delta}$ , prepared by solid-state reaction *in situ* without recourse to a reducing atmosphere.<sup>15</sup> Alternatively, decoration of the cathode with Ag NPs may be achieved through impregnation with wet solutions. Liu *et al.*<sup>16</sup> employed a citrate method to impregnate Ag NPs into a porous  $\text{La}_{0.6}\text{Sr}_{0.4}\text{Co}_{0.2}\text{Fe}_{0.8}\text{O}_{3-\delta}:\text{Ce}_{0.8}\text{Gd}_{0.2}\text{O}_{1.9}$  functional cathode, yielding high power densities for a microtubular SOFC. Alternatively, Su *et al.*<sup>17</sup> decorated  $\text{Ba}_{0.5}\text{Sr}_{0.5}\text{Co}_{0.6}\text{Fe}_{0.4}\text{O}_{3-\delta}$  electrodes by a vacuum-assisted electroless deposition technique.

We recently reported the promising cathode properties of  $\text{Nd}_{1/3}\text{Sr}_{2/3}\text{CoO}_{3-\delta}$ .<sup>18</sup> Here, we demonstrate for the first time the synthesis and deposition in a single step of  $(\text{Nd,Gd})_{1/3}\text{Sr}_{2/3}\text{CoO}_{3-\delta}:\text{Ce}_{0.9}(\text{Gd,Nd})_{0.1}\text{O}_{1.95}$  composite air electrodes decorated with Ag NPs by spray pyrolysis followed by a low-temperature sintering step. The composite air electrodes and Ag NPs are studied by XRD, EXAFS/XANES, HRTEM, and HAADF-STEM. The electrochemical polarisation performance of symmetrical cells of the air electrodes deposited on  $\text{Ce}_{0.9}\text{Gd}_{0.1}\text{O}_{1.95}$  (CGO) electrolyte are examined by impedance spectroscopy to delineate the advantageous effects of spray-pyrolysis deposition and Ag NPs, and current–voltage measurements of a single cell fuel-cell are employed to further demonstrate the potential of the composite air electrode with Ag NPs for SOFC applications.

## 2. Experimental

### 2.1. Processing of electrodes by spray pyrolysis

Thin-film layers of  $(\text{Nd,Gd})_{1/3}\text{Sr}_{2/3}\text{CoO}_{3-\delta}:\text{Ce}_{0.9}(\text{Gd,Nd})_{0.1}\text{O}_{1.95}$  composites (70 : 30, w : w) were synthesised and deposited by spray pyrolysis using a Holmarc HO-TH-04BT instrument from

an aqueous solution of stoichiometric amounts of  $\text{Ce}(\text{NO}_3)_3 \cdot 6\text{H}_2\text{O}$  (Aldrich 99.0%),  $\text{Gd}(\text{NO}_3)_3 \cdot 6\text{H}_2\text{O}$  (Aldrich 99.9%),  $\text{Nd}(\text{NO}_3)_3 \cdot 6\text{H}_2\text{O}$  (Aldrich 99.9%),  $\text{Sr}(\text{NO}_3)_2$  (Aldrich 99.0%), and  $\text{Co}(\text{NO}_3)_2 \cdot 6\text{H}_2\text{O}$  (Aldrich 98.0%), with total metal concentration 1.71 M and glycine (2.23 M) as the fuel. The oxidiser-to-fuel power ratio was fixed as 1 : 1.<sup>19</sup> For Ag-decorated composites, the appropriate amount of  $\text{AgNO}_3$  (Panreac 99.0% 0.12 M) was added to the solution in the ratio  $(\text{Nd,Gd})_{1/3}\text{Sr}_{2/3}\text{CoO}_{3-\delta}:\text{Ce}_{0.9}(\text{Gd,Nd})_{0.1}\text{O}_{1.95}:\text{Ag}$  (70 : 30 : 10 w : w : w) and the concentration of fuel adjusted. The solutions were sprayed either onto an inert, ceramic, heated  $\text{Al}_2\text{O}_3$ -based plate or onto pellets of CGO electrolyte, as detailed below. In all cases, the films were heat treated at 900 °C for 4 hours to improve phase crystallinity. The same procedure was used to prepare  $\text{Nd}_{1/3}\text{Sr}_{2/3}\text{CoO}_{3-\delta}$  for comparison with the same composition prepared by the ceramic method, in which solid reactants were mixed in an agate mortar and heated at high temperature to promote solid-state reaction.<sup>18</sup>

CGO : Ag 90 : 10 (w : w) composites were prepared by the same spray pyrolysis method for analysis by XANES and EXAFS.

### 2.2. Compositional, structural, and microstructural characterisation

Analysis of phase composition and crystal structure was performed employing XRD data collected using a Bruker D8 high-resolution diffractometer equipped with a Ge primary monochromator ( $\text{CuK}\alpha_1$  radiation,  $\lambda = 1.5406 \text{ \AA}$ ), and a LynxEye fast detector. Data-collection parameters (measured angular range, step size, and counting times) were selected to ensure sufficient resolution (step size lower than 1/10 of the FWHMs) and good statistics for the diffraction analysis. The instrumental contribution to line broadening was determined using NIST  $\text{LaB}_6$  standard reference material (SRM 660a;  $\mu = 1138 \text{ cm}^{-1}$ , linear absorption coefficient for  $\text{CuK}\alpha_1$  radiation). Structural and microstructural features were refined simultaneously by the Rietveld method using the FullProf software package.<sup>20</sup>

Analysis of the morphology and microstructure of composites and cells was performed with a Prisma-E Scanning Electron Microscope (SEM). The average Feret diameter of the particles ( $D$ ) was determined from the scanning electron micrographs using the software Image J (v1.52a).

X-ray Absorption Fine Structure (XAFS) was determined at different temperatures to estimate the oxidation state and thermal evolution of Ag at Branch A of the Spanish CRG-SpLine of the ESRF (European Synchrotron Radiation Facility). The spectra were acquired in fluorescence yield mode, averaging a minimum of 3 spectra for each sample in conditions achieving a good signal-to-noise ratio. Heating of a conventional reaction cell to 800 °C equipped with kapton windows was performed for catalysis experiments. XAFS data were treated employing standard procedures in the Demeter package.<sup>21</sup> The experimental spectra were fitted to two contributions: metallic silver and  $\text{Ag}(i)$  with variable weight as a function of temperature. The analysis of the extended EXAFS was performed using crystallographic data of  $\text{Ag}^{22}$  and  $\text{Ag}_2\text{O}^{23}$  from conventional databases.



Transmission electron microscopy (TEM), high resolution transmission electron microscopy (HRTEM) and scanning transmission electron microscopy (STEM) were conducted with a JEOL JEM ARM200cF microscope operating at 200 kV equipped with a condenser lens aberration corrector, granting a spatial resolution of 0.08 Å. Energy dispersive X-ray spectroscopy (EDS) was performed using a microanalysis system from OXFORD.

### 2.3. Electrical conductivity

Total electrical conductivity was determined by direct current (d.c.) four-electrode measurements of rectangular dense bars using an Autolab PGSTAT302N potentiostat/galvanostat. The bars were prepared by pressing the powders in a die at 200 MPa and sintering at 1100 °C for 12 hours. One pair of Pt-wire electrodes was attached to the external Pt-covered surfaces to conduct a direct current flux through the length of the bars in galvanostatic mode. Another pair of Pt wires was internally located on the bars to determine the voltage difference arising between parallel planes. Measurements were performed in air, O<sub>2</sub> and N<sub>2</sub> in the temperature range 150–950 °C on cooling in steps of 50 °C at a rate of 5 °C min<sup>-1</sup> after stabilisation for 15 min at each step. Equilibrium was assured by maintaining the samples under the corresponding atmospheres at 950 °C for 12 h before initiating measurements.

### 2.4. Electrochemical analysis

The electrochemical behaviour of air-electrode composites on CGO electrolyte was studied with symmetrical cells. High-density cylindrical electrolyte pellets were obtained by uniaxial pressing of CGO powder (Rhodia) to 125 MPa followed by sintering in air at 1400 °C for 10 h; relative density was >98% with diameter ~8 mm and thickness ~1.2 mm. For comparative purposes, symmetrical cells were prepared applying different processing methods. A (Nd,Gd)<sub>1/3</sub>Sr<sub>2/3</sub>-CoO<sub>3-δ</sub>:Ce<sub>0.9</sub>(Gd,Nd)<sub>0.1</sub>O<sub>1.95</sub> composite cathode (70 : 30, w : w) was prepared from powder obtained by spray pyrolysis on to a hot inert alumina plate at 500 °C, then heated at 900 °C, and mixed with a binder (Decoflux™, WB41, Zschimmer and Schwartz) to form a slurry, then deposited (slurry coated, SC) on opposite sides of CGO electrolyte pellets and fired at 900 °C for 3 hours. To obtain spray-pyrolysed electrodes of (Nd,Gd)<sub>1/3</sub>Sr<sub>2/3</sub>CoO<sub>3-δ</sub>:Ce<sub>0.9</sub>(Gd,Nd)<sub>0.1</sub>O<sub>1.95</sub> and silver-decorated composites (denoted as SP and SP\_Ag, respectively), the corresponding solutions were directly sprayed onto both faces of a CGO electrolyte pellet at 500 °C and fired in a furnace at 900 °C for 3 hours. In all cases, silver paste was applied by brushing on both pellet faces followed by drying at room temperature to serve as current collector. Impedance-spectroscopy measurements were carried out using an Autolab PGSTAT302N instrument with a FRA2 module, applying a signal amplitude of 50 mV in the frequency range 0.1–10<sup>6</sup> Hz. The impedance spectra were fitted to equivalent circuits using the Zview software.<sup>24</sup> The ASR values (associated to the total electrochemical processes at the electrodes) were determined from the corresponding

contribution of electrode polarisation resistance, according to the typical capacitances of the processes,<sup>25</sup> normalised for the electrode area and divided by 2 to account for both electrodes in the symmetrical cell set-up.<sup>2,26</sup>

### 2.5. Fuel-cell preparation and performance

To evaluate the performance of the most promising cathode composites under study ((Nd,Gd)<sub>1/3</sub>Sr<sub>2/3</sub>CoO<sub>3-δ</sub>:Ce<sub>0.9</sub>(Gd,Nd)<sub>0.1</sub>O<sub>1.95</sub>:Ag) in single fuel-cell operating conditions, anode-supported cells were fabricated. NiO : CGO (60 : 40 w : w) composite anodes were prepared by solution combustion on mixing stoichiometric amounts of Ni(NO<sub>3</sub>)<sub>2</sub>·6H<sub>2</sub>O (Sigma Aldrich 98.5%) and CGO powder (Rhodia). The water was slowly evaporated by heating under constant stirring then the remaining mixture was fired in an oven at 800 °C for 1 hour to decompose the nitrate to NiO. At this stage, an organic pore-forming agent was added (corn-starch powder, 15 vol%). The anode composite was then compacted into a disk-shaped membrane and pre-sintered at 1000 °C for 1 hour. Subsequently, inks of the YSZ and CGO electrolytes were prepared by mixing the powders with a binder (Decoflux) and deposited by slurry coating onto the NiO-CGO support. The anode-YSZ electrolyte assembly was then sintered at 1400 °C for 4 h to densify the YSZ electrolyte layer, followed by deposition and sintering of the CGO layer at 1250 °C. The Ag-decorated composite air electrode was deposited onto the exposed CGO electrolyte layer of the sintered anode-electrolyte assembly by spray-pyrolysis and fired at 900 °C for 3 hours.

To assess the fuel-cell performance, the single cell was sealed over a YSZ tube using Ceramabond 552 adhesive (Aremco). Ni : CGO cermet anode was obtained by *in situ* reduction of NiO under a H<sub>2</sub> flow rate of 75 ml min<sup>-1</sup> for 2 hours on the anode side. Current-voltage curves were acquired in the range 500–700 °C, with an Autolab PGSTAT302N potentiostat/galvanostat while a flow of dry H<sub>2</sub> was continuously supplied to the anode and static air to the cathode.

## 3. Results and discussion

### 3.1. Structural characterisation

We previously reported the synthesis of polycrystalline Nd<sub>1/3</sub>Sr<sub>2/3</sub>CoO<sub>3-δ</sub> by the ceramic method with a grain size in the order of several microns.<sup>18</sup> To facilitate processing, improve the electrode microstructure, and enhance electrochemical performance, spray-pyrolysis was employed to prepare (Nd,Gd)<sub>1/3</sub>Sr<sub>2/3</sub>CoO<sub>3-δ</sub>:Ce<sub>0.9</sub>(Gd,Nd)<sub>0.1</sub>O<sub>1.95</sub> composites (Ag-decorated and non-decorated). Fig. 1(a) presents the XRD pattern of a composite air electrode prepared by spray pyrolysis over a hot alumina plate, as previously described. According to the XRD results, the sample contains perovskite and fluorite oxides as the only phases. Rietveld refinement indicated a phase ratio of 69 : 31 (wt% perovskite : wt% fluorite). In addition, a small crystallite size of 72 and 51 nm for the perovskite and fluorite phases, respectively, was determined by line-broadening analysis (Table S1†). The small particle size and high porosity (see below) produces large specific surfaces and extended TPBs, which are favourable for the ORR.



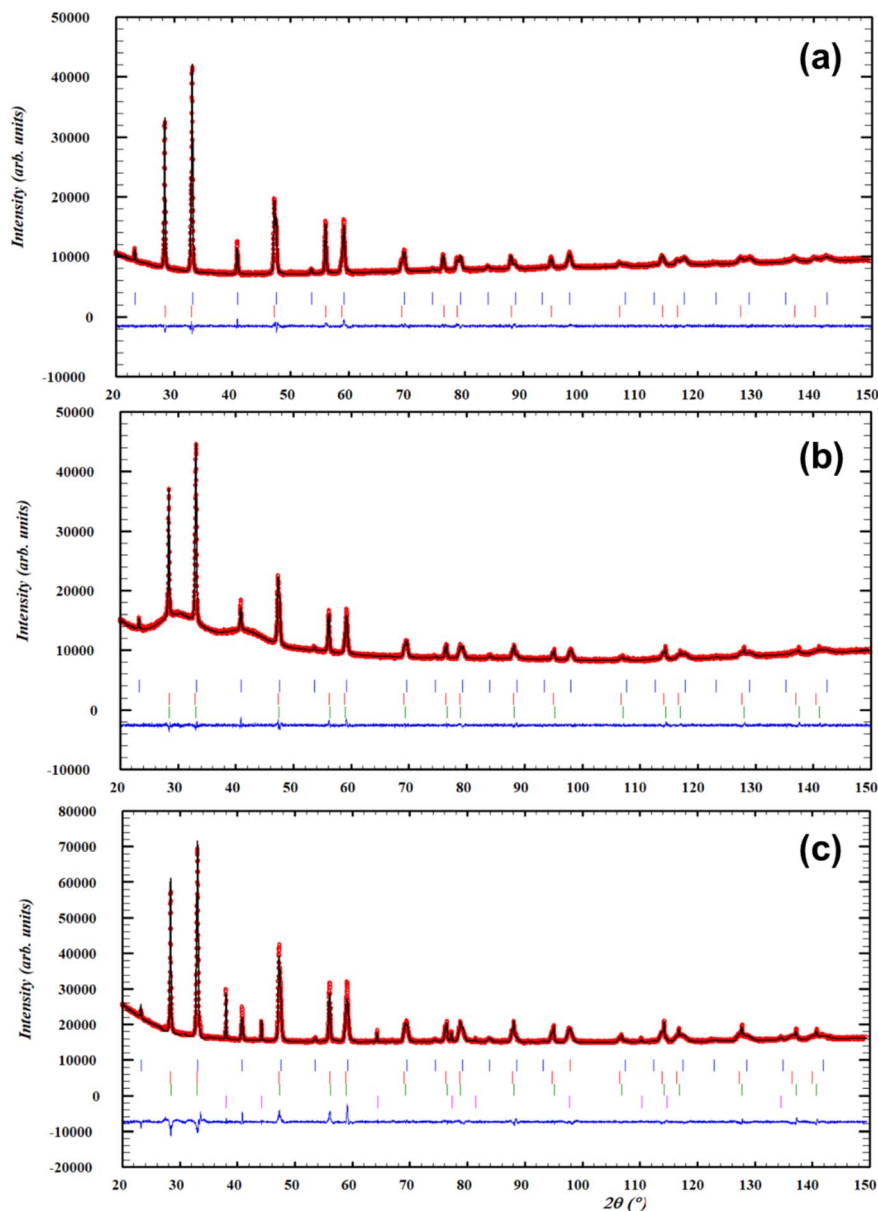


Fig. 1 Experimental (red points), calculated (solid black line) and their difference (blue line at bottom) laboratory XRD patterns at room temperature of (a) composite powder  $(\text{Nd,Gd})_{1/3}\text{Sr}_{2/3}\text{CoO}_{3-\delta}:\text{Ce}_{0.9}(\text{Gd,Nd})_{0.1}\text{O}_{1.95}$  prepared by spray-pyrolysis on a hot alumina plate, (b) composite  $(\text{Nd,Gd})_{1/3}\text{Sr}_{2/3}\text{CoO}_{3-\delta}:\text{Ce}_{0.9}(\text{Gd,Nd})_{0.1}\text{O}_{1.95}$  prepared and deposited by spray-pyrolysis onto a CGO pellet, (c) Ag-decorated composite  $(\text{Nd,Gd})_{1/3}\text{Sr}_{2/3}\text{CoO}_{3-\delta}:\text{Ce}_{0.9}(\text{Gd,Nd})_{0.1}\text{O}_{1.95}$  prepared and deposited by spray-pyrolysis onto a CGO pellet. In all cases the vertical bars indicate the positions of the Bragg peaks: blue,  $(\text{Nd,Gd})_{1/3}\text{Sr}_{2/3}\text{CoO}_{3-\delta}$ ; red,  $\text{Ce}_{0.9}(\text{Gd,Nd})_{0.1}\text{O}_{1.95}$  in composite; green, CGO pellet; fuchsia, Ag NPs.

Fig. 1(b) shows the XRD pattern of an  $(\text{Nd,Gd})_{1/3}\text{Sr}_{2/3}\text{CoO}_{3-\delta}:\text{Ce}_{0.9}(\text{Gd,Nd})_{0.1}\text{O}_{1.95}$  composite layer prepared *in situ* by spray pyrolysis on a CGO electrolyte pellet, in which  $(\text{Nd,Gd})_{1/3}\text{Sr}_{2/3}\text{CoO}_{3-\delta}$ ,  $\text{Ce}_{0.9}(\text{Gd,Nd})_{0.1}\text{O}_{1.95}$  in the composite and CGO of the substrate are detected. The corresponding structural and microstructural features of each phase are provided in Table S2† and indicate a slightly larger unit cell for  $\text{Ce}_{0.9}(\text{Gd,Nd})_{0.1}\text{O}_{1.95}$  in the composite in comparison to that of the electrolyte, although refined oxygen occupancies give similar values. The increase in lattice parameter is likely due to the introduction of Nd cations on Ce/Gd sites in the fluorite structure; the ionic radii of  $\text{Nd}^{3+}$  and  $\text{Gd}^{3+}$  are

1.27 Å and 1.21 Å, respectively. The partial substitution of Nd on fluorite cation sites was confirmed by Energy dispersive X-ray spectroscopy elemental maps, as discussed below. Nevertheless, the phase ratio of fluorite and perovskite phases is close to the expected nominal value. The calculated crystallite sizes in the composite are similar and nanometric in diameter, 65 nm and 66 nm for  $(\text{Nd,Gd})_{1/3}\text{Sr}_{2/3}\text{CoO}_{3-\delta}$  and  $\text{Ce}_{0.9}(\text{Gd,Nd})_{0.1}\text{O}_{1.95}$ , respectively. The XRD pattern of an Ag-decorated composite air electrode deposited by spray pyrolysis on a CGO electrolyte membrane is presented in Fig. 1(c). Similar to the above case, CGO from the electrolyte is observed, whereas the composite exhibits  $(\text{Nd,Gd})_{1/3}$



$\text{Sr}_{2/3}\text{CoO}_{3-\delta}$ ,  $\text{Ce}_{0.9}(\text{Gd,Nd})_{0.1}\text{O}_{1.95}$  and Ag NPs phases (Table S3†). The weight ratio of these phases is very close to the nominal values. The crystallite sizes of  $(\text{Nd,Gd})_{1/3}\text{Sr}_{2/3}\text{CoO}_{3-\delta}$  and  $\text{Ce}_{0.9}(\text{Gd,Nd})_{0.1}\text{O}_{1.95}$  in the composite are similar to the above-mentioned Ag-free case (Table S2†). However, the silver particles are considerably larger (150 nm), most likely because the post-spray thermal treatment is close to the Ag melting point, promoting particle growth.

To understand the electrochemical performance, scanning transmission electron microscopy (STEM) and elemental mapping analysis were employed to perform an in-depth study of the composition, morphology, and interaction among  $(\text{Nd,Gd})_{1/3}\text{Sr}_{2/3}\text{CoO}_{3-\delta}$ ,  $\text{Ce}_{0.9}(\text{Gd,Nd})_{0.1}\text{O}_{1.95}$  and Ag NPs. Fig. 2(a) shows a STEM image of the composite air electrode in which the primary particles of  $(\text{Nd,Gd})_{1/3}\text{Sr}_{2/3}\text{CoO}_{3-\delta}$

$\text{CoO}_{3-\delta}$  are very well connected to  $\text{Ce}_{0.9}(\text{Gd,Nd})_{0.1}\text{O}_{1.95}$  particles and both are decorated with Ag NPs. In Fig. 2(a), single particles of CGO (zone A) and  $(\text{Nd,Gd})_{1/3}\text{Sr}_{2/3}\text{CoO}_{3-\delta}$  (zone B) are highlighted. EDS elemental mapping of Ce, Gd and Nd, shown in blue, green and yellow, respectively, in Fig. 2(c)–(e), confirms that the fluorite particles (A) contain Nd, Gd and Ce, whereas the perovskite material (zone B) contains Gd, Nd, Sr (represented in orange) and Co (red), but not Ce (blue). The presence of Nd and Gd cations of similar ionic radii in both phases is not unexpected since the synthesis of both compounds is performed simultaneously by spray pyrolysis from the dissolved cation-precursor solutions. In addition, the EDS elemental mapping of Ce clearly indicates that this cation is not present in the  $(\text{Nd,Gd})_{1/3}\text{Sr}_{2/3}\text{CoO}_{3-\delta}$

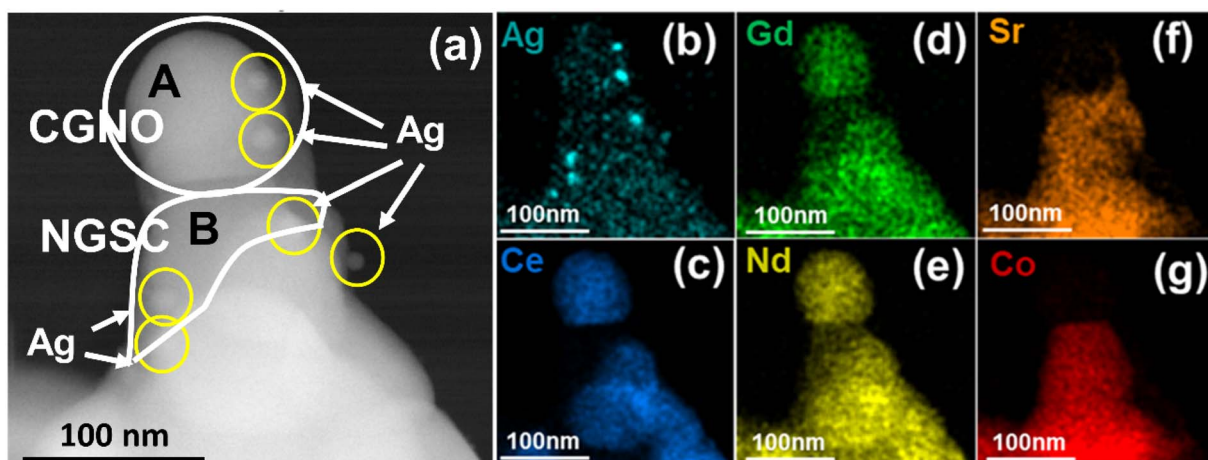


Fig. 2 (a) Low-magnification STEM image of  $(\text{Nd,Gd})_{1/3}\text{Sr}_{2/3}\text{CoO}_{3-\delta}:\text{Ce}_{0.9}(\text{Gd,Nd})_{0.1}\text{O}_{1.95}:\text{Ag}$  and EDS elemental maps corresponding to (b) Ag, (c) Ce, (d) Gd, (e) Nd, (f) Sr and (g) Co. A and B in (a) indicate  $\text{Ce}_{0.9}(\text{Gd,Nd})_{0.1}\text{O}_{1.95}$  (CGNO) and  $(\text{Nd,Gd})_{1/3}\text{Sr}_{2/3}\text{CoO}_{3-\delta}$  (NGSC) particles, respectively, with no other overlapping particle.

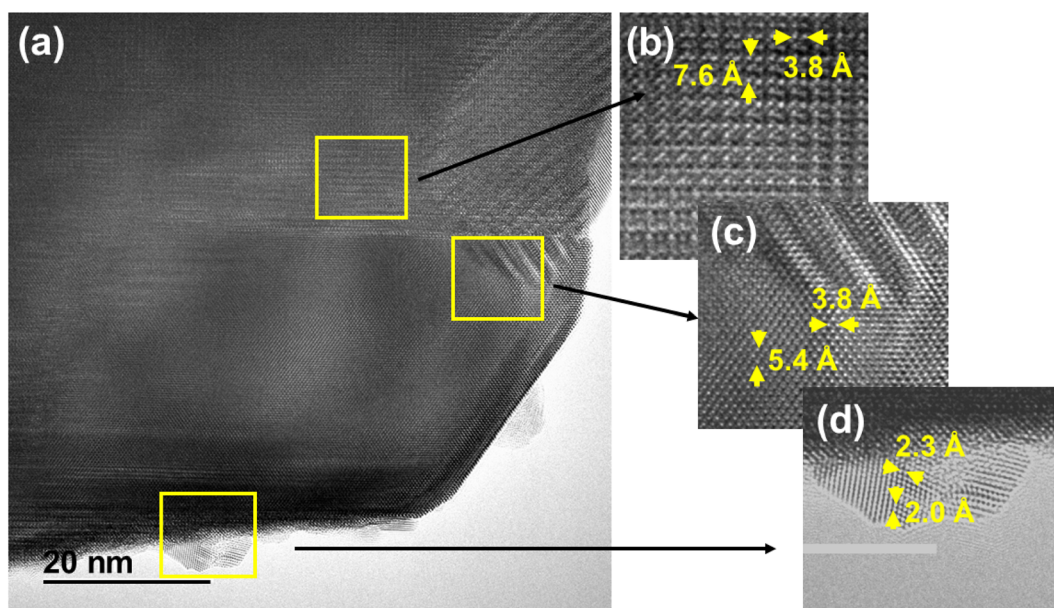


Fig. 3 (a) HRTEM image of Ag NPs decorated composite air electrode and enlarged images of (b)  $(\text{Nd,Gd})_{1/3}\text{Sr}_{2/3}\text{CoO}_{3-\delta}$ , (c)  $\text{Ce}_{0.9}(\text{Gd,Nd})_{0.1}\text{O}_{1.95}$  and (d) Ag NPs.



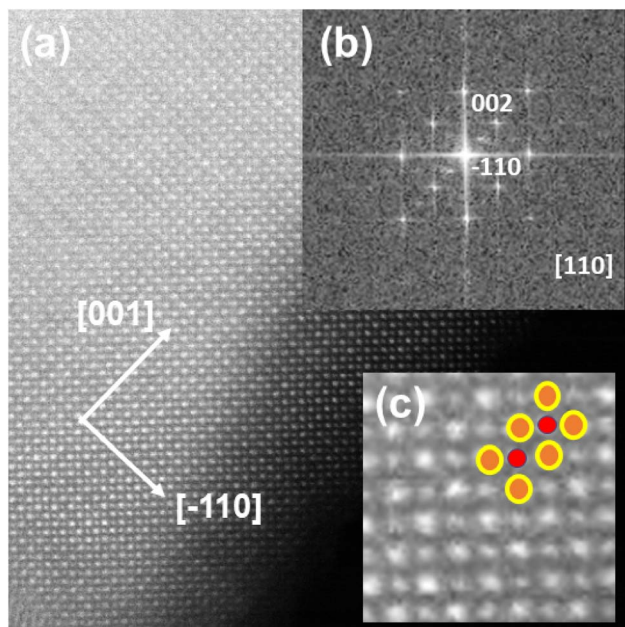


Fig. 4 HAADF-STEM image of (a)  $(\text{Nd,Gd})_{1/3}\text{Sr}_{2/3}\text{CoO}_{3-\delta}$  along the  $[110]$  direction, (b) corresponding optical Fourier-Transform image and (c) magnification of HAADF-STEM image, where relevant atoms are superimposed; Nd/Gd/Sr and Co are represented in yellow/orange and red, respectively.

$\text{CoO}_{3-\delta}$  phase (B zone). The EDS analysis confirms that there is no interdiffusion of the other elements between different phases.

The HRTEM image of the composite air electrode decorated with Ag NPs, Fig. 3, reveals high crystallinity of the three components. Atomic-level HRTEM analysis of the  $(\text{Nd,Gd})_{1/3}\text{Sr}_{2/3}\text{CoO}_{3-\delta}$  perovskite viewed from the  $[1-10]$  direction indicates interplanar distances of 7.6 and 3.8 Å, corresponding to (002) and (-110) planes, respectively. Lattice fringes of 5.4 and 3.8 Å confirm the presence of the fluorite structure, assignable to the (001) and (110) planes viewed along the  $[-110]$  direction. The presence of Ag NPs is confirmed by the lattice fringes of interplanar distances of 2.3 and 2.0 Å, corresponding, respectively, to (111) and (002) planes of Ag viewed along the  $[1-10]$  direction.

To elucidate the structure of  $(\text{Nd,Gd})_{1/3}\text{Sr}_{2/3}\text{CoO}_{3-\delta}$  in detail, HAADF (high-angle annular dark-field)-STEM imaging was performed, providing images of the crystal structure which, in most cases, are directly interpretable, although oxygen and other light elements may be barely visible in the presence of heavier atoms. A HAADF-STEM image along the  $[110]$  direction of  $(\text{Nd,Gd})_{1/3}\text{Sr}_{2/3}\text{CoO}_{3-\delta}$ , Fig. 4, reveals atomically resolved columns corresponding to Nd, Gd, Sr and Co (Fig. 4(c)), arranged in an ordered manner along the  $c$ -axis. The brightest diffraction spots correspond to the heaviest atoms (Nd, Gd and Sr) and the less intense reflections to Co; the Nd, Gd and Sr atoms appear to adopt a statistical distribution on the perovskite A site.

### 3.2. Morphology of spray-pyrolysed air electrodes

Spray pyrolysis provides a morphology consisting of nanometric or sub-micron grains sintered to form a scaffold of high porosity and tortuosity (Fig. 5(a)–(c)). In contrast,  $\text{Nd}_{1/3}\text{Sr}_{2/3}\text{CoO}_{3-\delta}$

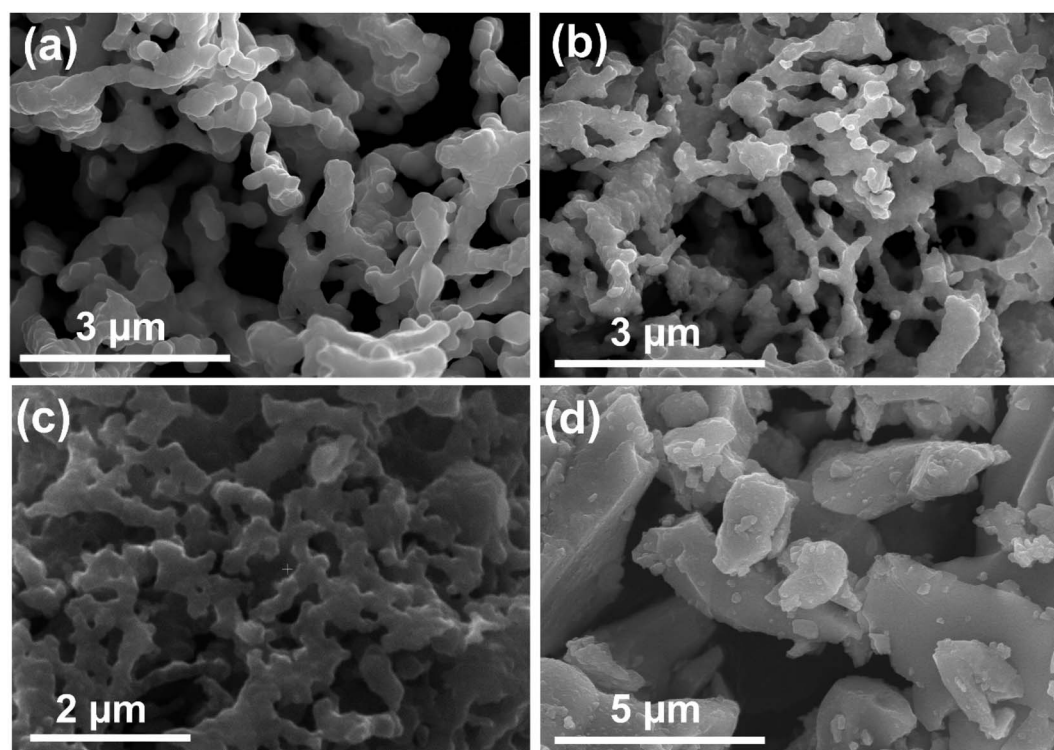


Fig. 5 Scanning electron microscopy images of (a)  $\text{Nd}_{1/3}\text{Sr}_{2/3}\text{CoO}_{3-\delta}$  prepared by spray-pyrolysis; (b)  $(\text{Nd,Gd})_{1/3}\text{Sr}_{2/3}\text{CoO}_{3-\delta}:\text{Ce}_{0.9}(\text{Gd,Nd})_{0.1}\text{O}_{1.95}$  prepared by spray-pyrolysis; (c)  $(\text{Nd,Gd})_{1/3}\text{Sr}_{2/3}\text{CoO}_{3-\delta}:\text{Ce}_{0.9}(\text{Gd,Nd})_{0.1}\text{O}_{1.95}:\text{Ag}$  prepared by spray-pyrolysis; (d)  $\text{Nd}_{1/3}\text{Sr}_{2/3}\text{CoO}_{3-\delta}$  prepared by the ceramic method.<sup>18</sup>



prepared by the ceramic method results in a grain size of several microns, as reported in our previous work (Fig. 5(d)).<sup>18</sup>

It is known that metal nanoparticles may melt or even evaporate at temperatures well below the melting point of the bulk metal. In the case of silver, according to Feng *et al.*,<sup>27</sup> the melting temperature of silver nanoparticles of 80 nm diameter is about 950 °C. Since the composites (Nd,Gd)<sub>1/3</sub>Sr<sub>2/3</sub>CoO<sub>3-δ</sub>:Ce<sub>0.9</sub>(Gd,Nd)<sub>0.1</sub>O<sub>1.95</sub>:Ag have been treated and tested at a maximum temperature of 900 °C, it is expected that the Ag NPs are present in our electrodes during the whole experimental procedure. This is a relevant point to consider for the widely adopted strategy of decoration of SOFC electrodes with Ag NPs.<sup>12–17</sup>

### 3.3. Oxidation state, core-shell structure, and thermal evolution of Ag particles

Silver metal is a good ORR catalyst since Ag–O interactions are sufficiently strong for O–O bond cleavage to occur, but weak enough to ensure rapid desorption of oxide anions formed by facile electron transfer from silver to oxygen atoms; the oxide ions then diffuse into the bulk of the ionic- or mixed-conducting component.<sup>28</sup> The structure of the surface plays an important role in the ORR process. A thin layer of oxide (or even a few Ag–O defects on the surface) is highly beneficial as it favours oxygen solution and diffusion into the metal core, resulting in an enhancement of catalytic activity for the ORR.<sup>29</sup> Moreover, a core-shell structure of metal nanoparticles hinders agglomeration and facilitates metal dispersion throughout the sample. Core-shell silver nanoparticles have been previously produced using SiO<sub>2</sub> as a protective layer, Ag@SiO<sub>2</sub>, but this shell may limit the activity of the metal particles.<sup>30–33</sup> The durability of the core-shell structure of catalytic particles is of paramount importance for long-term fuel-cell operation.

Composites of CGO:Ag were prepared for XANES to determine the oxidation state, core-shell structure and thermal evolution of Ag in the decorated electrodes. The XRD pattern and HRTEM images of the composite are provided in Fig. S1 and S2,<sup>†</sup> respectively. XRD confirms that the only phases present are CGO and metallic silver; HRTEM (Fig. S2<sup>†</sup>) indicates that both Ag and CGO are crystalline (characteristic *d*-spacings are marked in the figure) and the size of the Ag NPs is ~80 nm diameter.

**3.3.1 Silver oxidation state.** Ag K-edge XANES spectra, Fig. 6, were compiled from the composite and two standards Ag (Ag(0)) and Ag<sub>2</sub>O (Ag(I)) for the study of local structure. The best least-square fitting (LSF) of the Ag spectrum in the composite (red line in Fig. 6) using the spectra of Ag and Ag<sub>2</sub>O as components results in a weight composition of 83(2)% and 17(2)% of metallic silver and Ag<sub>2</sub>O, respectively.

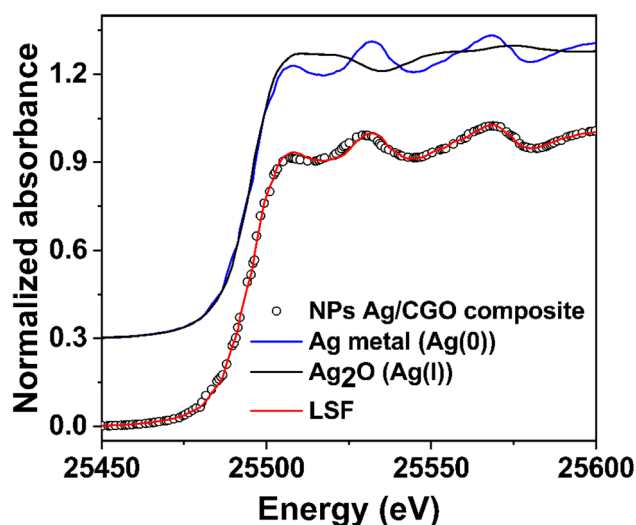


Fig. 6 Ag K-edge XANES spectra of the Ag/CGO composite material (open black circles), metallic silver (blue line) and silver oxide (black line). The best fit of the experimental spectrum of the composite (red line) reveals the presence of Ag and Ag<sub>2</sub>O.

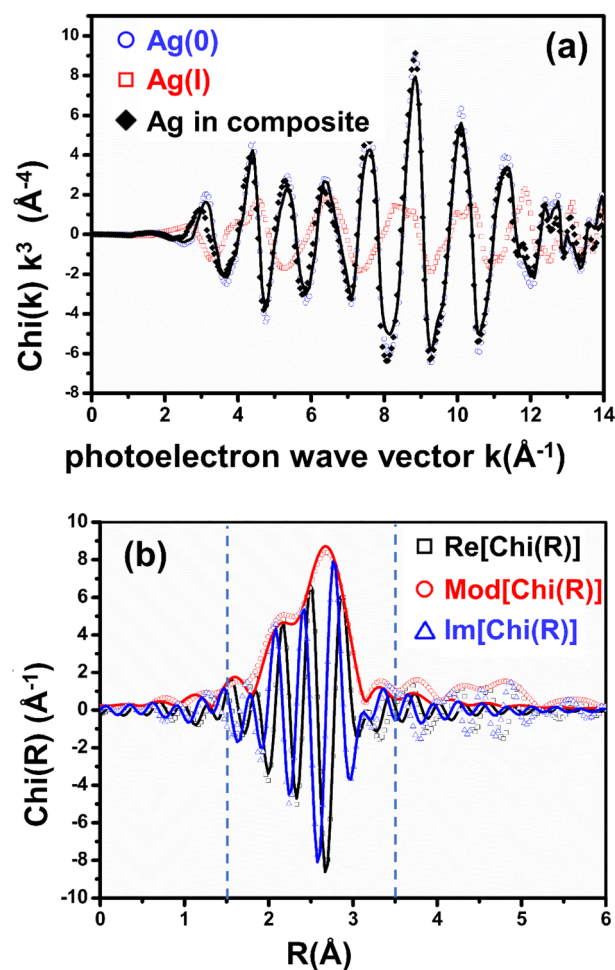


Fig. 7 EXAFS spectra of the Ag nanoparticles in the composite and metallic Ag and Ag<sub>2</sub>O references: (a) EXAFS as a function of the photoelectron wave-vector, including the best fit employing ITFA (continuous line); (b) Fourier Transform of the EXAFS spectrum of the Ag NPs in the composite (in the module, real and imaginary parts of the signal) and best fits (continuous lines of the corresponding colours) employing a binary phase system of composition 15% Ag<sub>2</sub>O and 85% Ag(0).



The reduced EXAFS signal of the silver nanoparticles in the composite, together with  $\text{Ag}_2\text{O}$  and Ag reference spectra, are shown in Fig. 7(a) as a function of the photoelectron wave-vector ( $k$ ). The EXAFS signal of Ag NPs presents more similarities to that of the Ag(0) standard. However, a clear displacement with respect to the signal of the metallic phase at the low-wavenumber region is observed, as a consequence of a significant contribution of oxygen in the first neighbouring shell (from the oxide).

A component analysis using the reduced EXAFS signals by iterative transformation factor analysis (ITFA)<sup>29</sup> was performed.

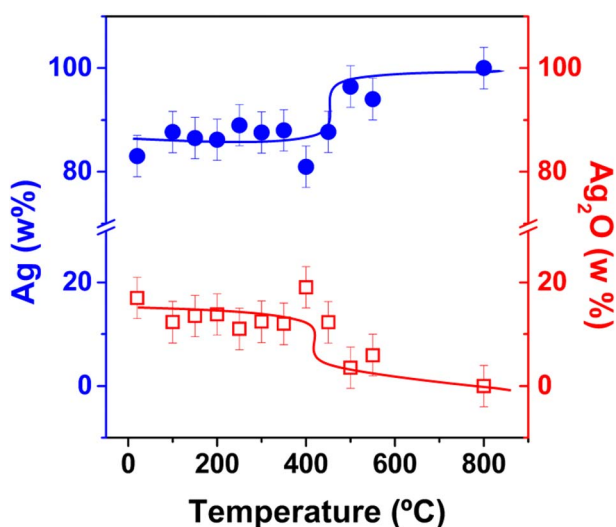


Fig. 8 Evolution of the phase composition of core-shell  $\text{Ag@Ag}_2\text{O}$  nanoparticles as a function of temperature in air (Ag and  $\text{Ag}_2\text{O}$  indicated as solid circles and open squares, respectively). Lines are guides for the eye.

The experimental signal is adjusted using a two-component model with  $\text{Ag}_2\text{O}$  and Ag references. The fit by this method (continuous line) adjusts to the NPs in the composite for a phase composition 13(5)/87(5)% of  $\text{Ag}_2\text{O}/\text{Ag}$ . In parallel, a standard EXAFS fitting (Fig. 7(b)) is performed using the same phase mixture ( $\text{Ag}/\text{Ag}_2\text{O}$ ), resulting in a phase composition of 15(5)/85(5). The robustness of the calculations to estimate the phase composition of the nanoparticles is supported by the good agreement of the results using these three methods (XANES-LCF, ITFA and EXAFS).

**3.3.2 Core-shell  $\text{Ag@Ag}_2\text{O}$  structure of as-prepared composite.** It is well known that the surface of metal nanoparticles oxidises rapidly in atmospheric conditions forming a passivation layer and core-shell structure. Silver is especially prone to oxidation; therefore, it can be assumed that the oxide phase observed in the XANES spectrum is due to surface oxidation and core-shell structure formation. The width of the outer  $\text{Ag}_2\text{O}$  layer may be determined using simple geometrical calculations, assuming the particles are spherical, adopting the  $\text{Ag}/\text{Ag}_2\text{O}$  weight ratio determined from XANES and the structural information (including density) for both phases; details of this calculation are given in ESI.† The result suggests that the outer particle shell consists of 1 unit cell of  $\text{Ag}_2\text{O}$  (unit cell parameter is 0.473 nm).<sup>23</sup>

The thin  $\text{Ag}_2\text{O}$  layer likely rationalises the absence of significant observed effects in the local structure of the nanometric particles, such as lattice collapse or amorphisation.<sup>34,35</sup> Nevertheless, the decrease in intensity of the Ag white-line of the XANES data in the composite in comparison to that of the bulk metallic standard provides evidence of the small particle size, since small metal particles present a distorted electronic structure with incomplete d orbitals with respect to the bulk state, diminishing the white-line intensity.

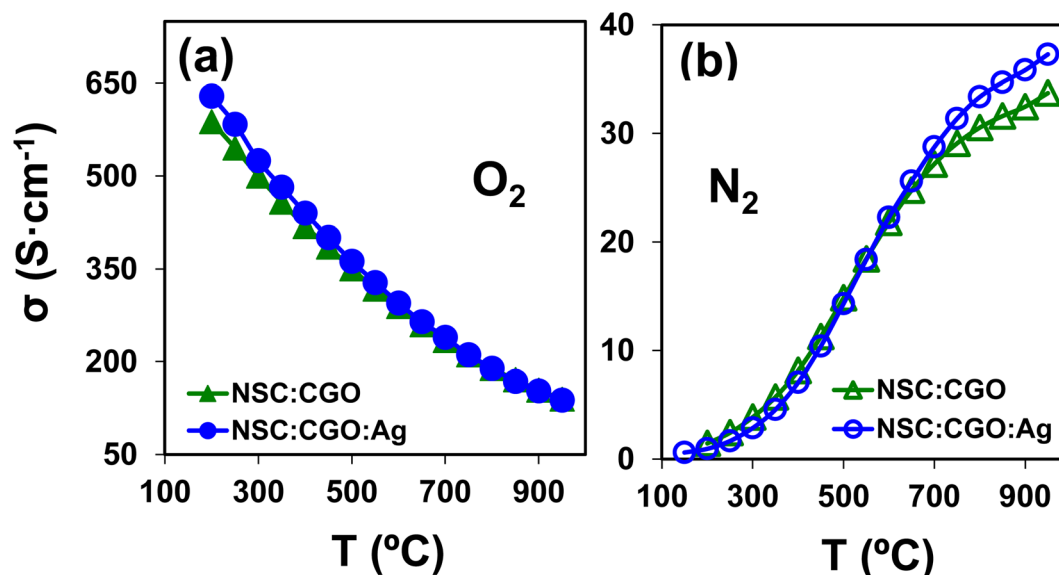


Fig. 9 Electrical conductivity as a function of temperature for  $(\text{Nd,Gd})_{1/3}\text{Sr}_{2/3}\text{CoO}_{3-\delta}:\text{Ce}_{0.9}(\text{Gd,Nd})_{0.1}\text{O}_{1.95}$  composite (triangles) and  $(\text{Nd,Gd})_{1/3}\text{Sr}_{2/3}\text{CoO}_{3-\delta}:\text{Ce}_{0.9}(\text{Gd,Nd})_{0.1}\text{O}_{1.95}:\text{Ag}$  (circles) composites in (a)  $\text{O}_2$  (flow rate of  $50 \text{ ml min}^{-1}$ ) and (b)  $\text{N}_2$  (flow rate of  $50 \text{ ml min}^{-1}$ ).





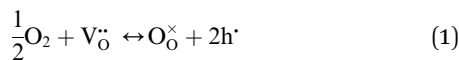
Table S4† summarises the EXAFS parameters obtained from the fittings and structural parameters for bulk Ag and Ag nanoparticles in the composite. We note that the reduction of coordination number of Ag in the composite is in good agreement with the formation of Ag nanoparticles.<sup>36–38</sup> The reduction of bond length is another well-known effect for metals in nanometric structures, which, in the case of the current composites, is around 1% reduction with respect to the bulk.

**3.3.3 Thermal evolution of the core-shell structure.** The thermal evolution of the relative phase composition of silver nanoparticles was determined on fitting a series of EXAFS spectra with increasing temperature from RT to 800 °C (Fig. 8). The Ag<sub>2</sub>O content remains constant on heating in the range RT – 450 °C. Beyond this temperature, Ag<sub>2</sub>O starts to decompose, as expected for noble-metal oxides.<sup>39</sup>

Hence, almost all the silver oxide on the surface of the nanoparticles is likely to be decomposed to metallic silver at the IT-SOFC working temperature of 700 °C with concomitant loss of the core-shell structure. However, local oxide defects on the particle surfaces may remain and improve ORR at higher temperatures.

### 3.4. Electrical and electrochemical properties

**3.4.1 Total conductivity.** The dc electrical conductivity of the Ag-decorated and non-decorated (Nd,Gd)<sub>1/3</sub>Sr<sub>2/3</sub>CoO<sub>3-δ</sub>:Ce<sub>0.9</sub>(Gd,Nd)<sub>0.1</sub>O<sub>1.95</sub> composites as a function of temperature under O<sub>2</sub> and N<sub>2</sub> atmospheres is similar for the two compositions (Fig. 9), with much higher conductivity registered in the more oxidising atmosphere due to the formation of electron-hole charge carriers, according to eqn (1):



The conductivity of (Nd,Gd)<sub>1/3</sub>Sr<sub>2/3</sub>CoO<sub>3-δ</sub>:Ce<sub>0.9</sub>(Gd,Nd)<sub>0.1</sub>O<sub>1.95</sub> in O<sub>2</sub> decreases progressively on heating due to loss of oxygen and electron holes, resulting in a shift in the defect equilibrium of eqn (1) to the creation of oxygen vacancies and concomitant reduction of Co<sup>4+</sup> to Co<sup>3+</sup>.<sup>18</sup> Conductivity under N<sub>2</sub> is clearly lower than that in O<sub>2</sub>, because the lower pO<sub>2</sub> (by 4–5 orders of magnitude) decreases drastically the electron-hole concentration (eqn (1)). The non-electronically conducting nature of Ce<sub>0.9</sub>(Gd,Nd)<sub>0.1</sub>O<sub>1.95</sub> in N<sub>2</sub> and O<sub>2</sub> atmospheres results in a considerable decrease of total conductivity of the (Nd,Gd)<sub>1/3</sub>Sr<sub>2/3</sub>CoO<sub>3-δ</sub>:Ce<sub>0.9</sub>(Gd,Nd)<sub>0.1</sub>O<sub>1.95</sub> composite compared to pure Nd<sub>1/3</sub>Sr<sub>2/3</sub>CoO<sub>3-δ</sub>.<sup>18</sup> Conductivity increases with temperature in N<sub>2</sub> due to the higher mobility of holes, typical of thermally activated conduction. The Ag NPs have little effect on the conductivity because the low Ag content is below the percolation threshold for parallel electrical conduction.

**3.4.2 Electrochemical performance of symmetrical cells.** The electrode polarisation resistances (*R<sub>p</sub>*) of symmetrical cells of all composite air electrodes deposited by slurry coating and/or spray-pyrolysis were determined by impedance spectroscopy in the range 500–700 °C (Fig. 10); the ohmic resistance of the electrolyte contribution has been subtracted in the figure for

easier comparison of the electrochemical response. The overall polarisation resistances are strongly dependent on both the deposition method and the presence of Ag nanoparticles: the *R<sub>p</sub>* values in air at 500 °C of the SC, SP and SP-Ag electrodes are 4.08, 3.07 and 1.35 Ω cm<sup>2</sup> (Fig. 10(a)), respectively, and 0.08, 0.04 and 0.03 Ω cm<sup>2</sup> at 700 °C, respectively (Fig. 10(c)). Hence,

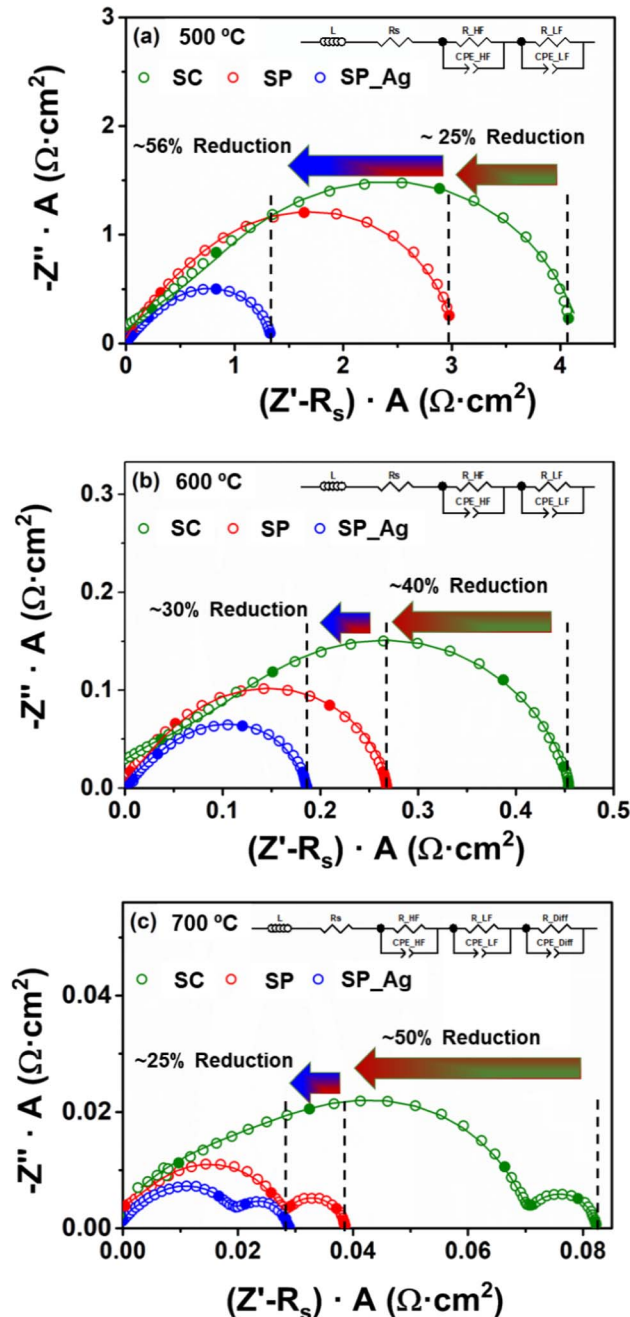


Fig. 10 Nyquist plots of symmetrical cells with composite cathodes deposited on CGO electrolyte, at (a) 500 °C, (b) 600 °C and (c) 700 °C, after subtraction of the ohmic contribution for electrodes prepared by slurry coating (SC), spray pyrolysis (SP) and Ag-decorated spray pyrolysis (SP-Ag). Solid lines represent the calculated spectra using the equivalent circuits indicated in the insets. Note that *R<sub>s</sub>* corresponds to the series resistance and that the impedance response was divided by 2 to account for the symmetric configuration.



spray-pyrolysis deposition and Ag-decoration diminish  $R_p$ , but the magnitude of each effect depends on temperature. The reduction in  $R_p$  for electrodes deposited by spray pyrolysis compared to slurry coating is  $\sim 40\text{--}50\%$  at  $600\text{ }^\circ\text{C}$  and above (Fig. 10(b) and (c)), whereas at  $500\text{ }^\circ\text{C}$  it decreases by  $\sim 25\%$  (Fig. 10(a)). In contrast, the reduction of  $R_p$  with Ag-nanoparticle decoration in samples prepared by spray pyrolysis is approximately  $56\%$  at the low temperature (Fig. 10(a)), whereas the effect is less pronounced ( $\sim 25\text{--}30\%$ ) at  $600$  and  $700\text{ }^\circ\text{C}$  (Fig. 10(b) and (c)). Both results agree with previous reports on the effect of silver on the electrochemical performance of metal oxides.<sup>14,40</sup>

The impedance spectra were fitted to appropriate equivalent circuits (insets of Fig. 10) to analyse and separate the different contributions to  $R_p$ . The equivalent circuits between  $500\text{--}650\text{ }^\circ\text{C}$  consist of an inductor ( $L$ ) attributed to the autoinduction process created at high frequency in the experimental setup, a series resistor ( $R_s$ ) to account for the ohmic resistance of the cell and two serial (R-CPE) elements corresponding to the electrochemical processes at high and low frequencies ( $R$  = resistance, CPE = constant phase element with impedance  $Q^{-1}(i\omega)^{-n}$ , where  $Q$  is the pseudo-capacitance and the exponent  $n$  lies in the range  $0 \leq n \leq 1$ ; for an ideal capacitor,  $n = 1$ ). In mixed-conducting cathodes without gas-diffusion limitations, it is widely accepted that the polarisation resistance at high

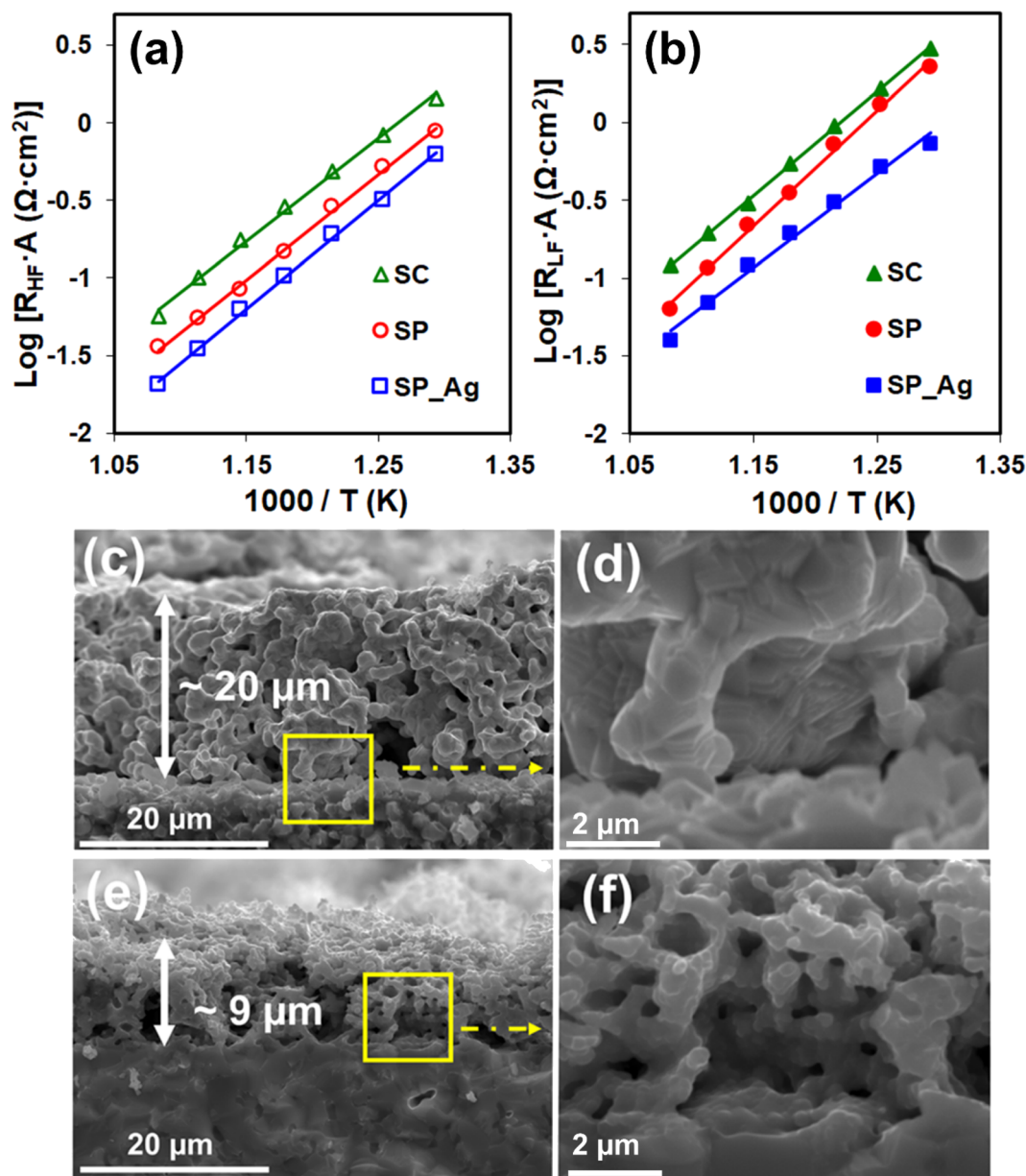


Fig. 11 Temperature dependence of electrochemical resistance associated with the high-frequency (a) and low-frequency (b) processes of the impedance spectra for the composite cathodes on CGO electrolyte. Scanning electron microscopy images of  $(\text{Nd,Gd})_{1/3}\text{Sr}_{2/3}\text{CoO}_{3-\delta}:\text{Ce}_{0.9}(\text{Gd,Nd})_{0.1}\text{O}_{1.95}$  electrodes obtained by (c) and (d) slurry coating and (e) and (f) spray-pyrolysis.



frequencies (HF) is related to ion diffusion, whereas the low-frequency (LF) resistance is associated with oxygen absorption, diffusion and reduction at the surface.<sup>41</sup> Between 500–650 °C, all the capacitance values are around  $10^{-4}$  F cm<sup>2</sup> for the high-frequency process and in the range of  $10^{-2}$  F cm<sup>2</sup> for the low-frequency process, which confirms that all contributions present in the spectra are related to the electrode. We note that, at 700 °C, a further (R-CPE) element at low frequencies is required to model the diffusion process of O<sub>2</sub> molecules through the electrode (denoted as (R-CPE)<sub>diff</sub>). From the R-CPE values, the capacitance (*C*) and relaxation frequency (*f<sub>r</sub>*) may be calculated using eqn (2)–(4):

$$C = \frac{(RQ)^{\frac{1}{n}}}{R}; \quad (2)$$

$$f_r = \frac{\omega_r}{2\pi}; \quad (3)$$

$$\omega_r = (RQ)^{-\frac{1}{n}} \quad (4)$$

where  $\omega_r$  corresponds to the angular relaxation frequency.

The Arrhenius representation of the HF and LF polarisation-resistance contributions, Fig. 11(a), shows that the activation energy of the HF process is similar for different samples (1.31–1.38 eV); however, the resistance is much lower for electrodes deposited by spray pyrolysis, likely attributable to the smaller particle size and corresponding increase of the active reaction surface associated with the synthesis and deposition method (the SEM images of cell cross-sections with composite air electrodes

deposited by the two methods are shown in Fig. 11(c) and (e)). For both spray pyrolysis and slurry deposition, the different phases are homogeneously distributed, as revealed by elemental distribution analysis (Fig. S3†). The electrodes deposited by slurry coating have a thickness of  $\sim 20$   $\mu\text{m}$ , present good porosity and are constituted by particle aggregates of approximately 1250 nm in diameter (Fig. 11(c) and (d)). However, the electrodes prepared and deposited by spray pyrolysis are of much lower thickness,  $\sim 9$   $\mu\text{m}$ , higher porosity, and much lower average grain size of 550 nm (Fig. 11(e)). A higher magnification image, Fig. 11(f), confirms that the SP electrode is formed by well-sintered particles with smaller size compared to slurry coating, leading to better electrode/electrolyte contact. These characteristics improve charge transfer at the electrode/electrolyte interface and minimise cation interdiffusion between adjacent components. On the other hand, the LF electrochemical process is significantly improved with the Ag nanoparticles (Fig. 11(b)). Moreover, the activation energy of the LF resistance is clearly lower for the

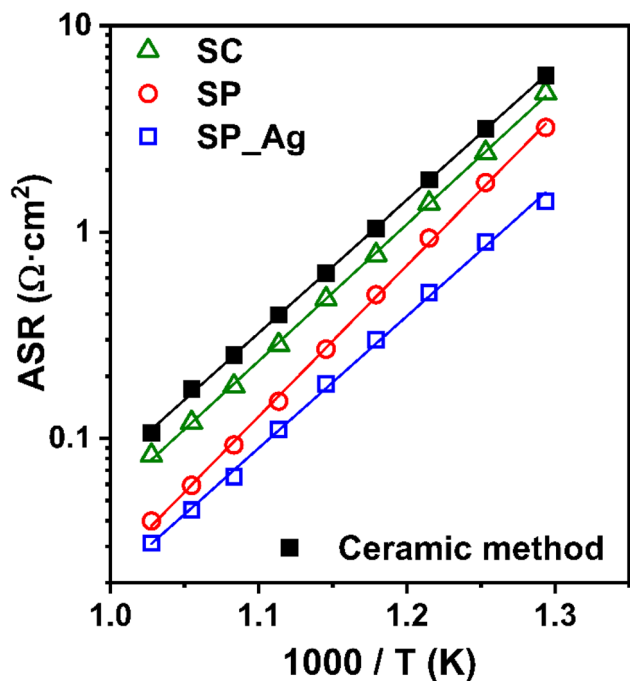


Fig. 12 Arrhenius plot of area-specific electrode polarisation resistance obtained from the impedance spectra of symmetrical cells. The results of Nd<sub>1/3</sub>Sr<sub>2/3</sub>CoO<sub>3- $\delta$</sub>  prepared by the ceramic method and deposited by slurry coating are included for comparison.<sup>18</sup>

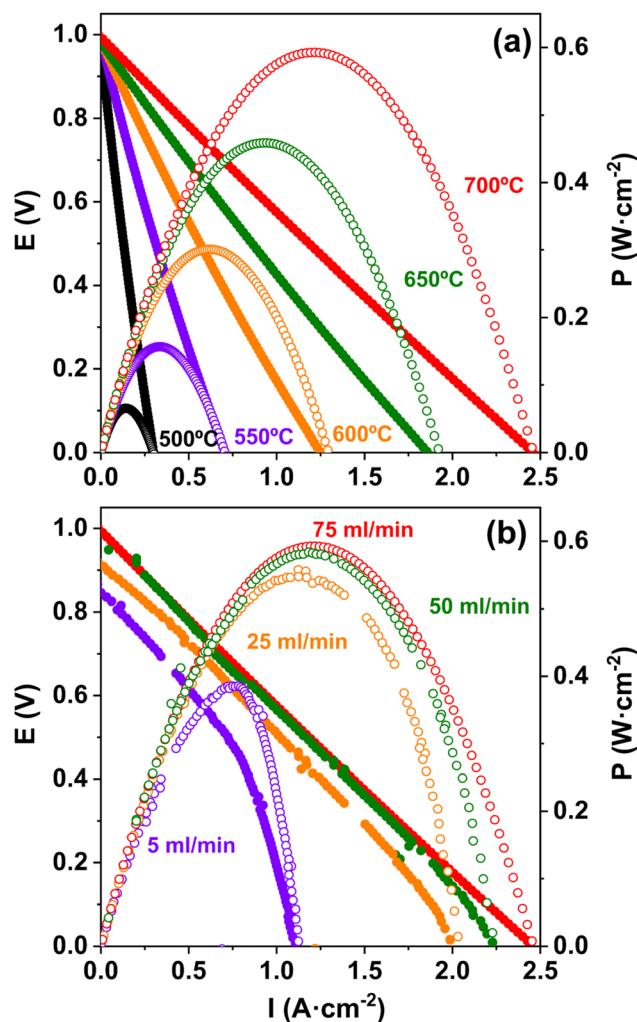


Fig. 13 (a) Fuel-cell performance of an anode-supported single cell based on Ni-CGO/YSZ/CGO/(Nd,Gd)<sub>1/3</sub>Sr<sub>2/3</sub>CoO<sub>3- $\delta$</sub> :Ce<sub>0.9</sub>(Gd,Nd)<sub>0.1</sub>O<sub>1.95</sub>:Ag using H<sub>2</sub> (flow rate: 75 ml min<sup>-1</sup>) as fuel and static air as oxidant; (b) fuel-cell performance of Ni-CGO/YSZ/CGO/(Nd,Gd)<sub>1/3</sub>Sr<sub>2/3</sub>CoO<sub>3- $\delta$</sub> :Ce<sub>0.9</sub>(Gd,Nd)<sub>0.1</sub>O<sub>1.95</sub>:Ag as a function of H<sub>2</sub> rate flow.



SP\_Ag electrode ( $E_a = 1.19$  eV) in comparison to the other composites (1.32–1.45 eV), leading to a greater improvement of the corresponding electrochemical process in the low-temperature range. In mixed-conducting cathodes, the electrochemical activity is highly influenced by the oxygen-vacancy concentration, due to its direct effect on both the oxygen surface exchange and oxide-ion diffusion.<sup>42</sup> The oxygen-vacancy content in  $(\text{Nd,Gd})_{1/3}\text{Sr}_{2/3}\text{CoO}_{3-\delta}$  decreases considerably as temperature decreases, as confirmed by the oxygen uptake observed by thermogravimetric analysis.<sup>18</sup> This contributes to the deterioration of the electrochemical activity at lower temperatures, leading to high activation-energy values. However, the presence of Ag NPs favours oxygen absorption and reduction, improving the electrochemical LF process and cathode performance, as observed previously.<sup>12–14</sup> This effect is more prominent in the low-temperature range, where the oxygen surface exchange is inhibited by the lower oxygen-vacancy content.

The effect of temperature on the electrode polarisation resistances ( $R_p$ ) for all composites is plotted in Fig. 12. The data for a composite air electrode prepared by the ceramic method and slurry coated on CGO (as previously reported in ref. 18) are included for comparison. The results confirm that the preparation of composites by spray pyrolysis on a hot alumina plate decreases the electrode polarisation resistance in comparison to those prepared by the ceramic method.<sup>18</sup> This is likely attributable to the lower processing temperature of spray pyrolysis which extends the active surface area, in addition to minimising interdiffusion between adjacent cell components.<sup>8</sup> Moreover, Fig. 12 shows that spray-pyrolysis deposition lowers the total electrode polarisation resistance in comparison to slurry coating, which results from both high- and low-frequency processes (Fig. 10 and 11). In this regard, the electrode polarisation resistance of the SP\_Ag electrode is clearly lower than that of the other composites, with the difference greater in the lower temperature range, because of the effect of the Ag NPs lowering the LF contribution. It is well established that, in oxidising conditions, a thin layer of silver oxide forms on the metal-particle

surfaces through which oxygen can absorb and diffuse, thereby improving the ORR.<sup>28,29</sup> The decomposition of this thin silver oxide layer as temperature rises (Fig. 8) diminishes the effect of Ag NPs on the oxygen electrochemical reaction at higher temperatures.

### 3.5. Fuel-cell performance

Fig. 13(a) shows the current density–voltage and current density–power density curves of single fuel cells corresponding to the Ag-decorated composite air electrode with YSZ and CGO as electrolyte bilayer, operating with an  $\text{H}_2$  flow rate of  $75 \text{ ml min}^{-1}$  at the anode and static air at the cathode. The open-circuit voltage at 500, 600 and 700 °C is approximately 1.00 V, similar to values previously reported in the literature for analogous thin bilayer electrolytes based on YSZ/CGO,<sup>43</sup> suggesting good sealing and good electrolyte density. The maximum power densities of the cell are  $0.07$ ,  $0.3$  and  $0.6 \text{ W cm}^{-2}$  at 500, 600 and 700 °C, respectively. The modification of the  $\text{H}_2$  flow rate in the range  $25$ – $75 \text{ ml min}^{-1}$  (Fig. 13(b)) leads to significant changes in the cell performance, decreasing considerably for values lower than  $25 \text{ ml min}^{-1}$  for which high current demands are limited due to mass-transport polarisation. Total cell resistances of  $\sim 0.4$  and  $0.75 \Omega \text{ cm}^{-2}$  at 700 °C and 600 °C, respectively, are inferred from Fig. 13(a), suggesting that the main sources of voltage loss are not attributable to electrochemical polarisation of the cathode (Fig. 10). Hence, there is considerable potential for further improvement of cell performance with the employed composition and processing methodology.

Scanning electron microscopy images (Fig. 14(a)) reveal the morphology of the cross section of the NiO-CGO/YSZ/CGO/ $(\text{Nd,Gd})_{1/3}\text{Sr}_{2/3}\text{CoO}_{3-\delta}:\text{Ce}_{0.9}(\text{Gd,Nd})_{0.1}\text{O}_{1.95}:\text{Ag}$  single cell, with a highly dense YSZ electrolyte of average thickness  $\sim 10 \mu\text{m}$ , a porous CGO interlayer of thickness  $\sim 15 \mu\text{m}$  and a porous  $(\text{Nd,Gd})_{1/3}\text{Sr}_{2/3}\text{CoO}_{3-\delta}:\text{Ce}_{0.9}(\text{Gd,Nd})_{0.1}\text{O}_{1.95}:\text{Ag}$  composite air electrode layer of thickness  $\sim 15 \mu\text{m}$ . The anode (Ni-CGO) and cathode both exhibit good porosity and particle homogeneity.

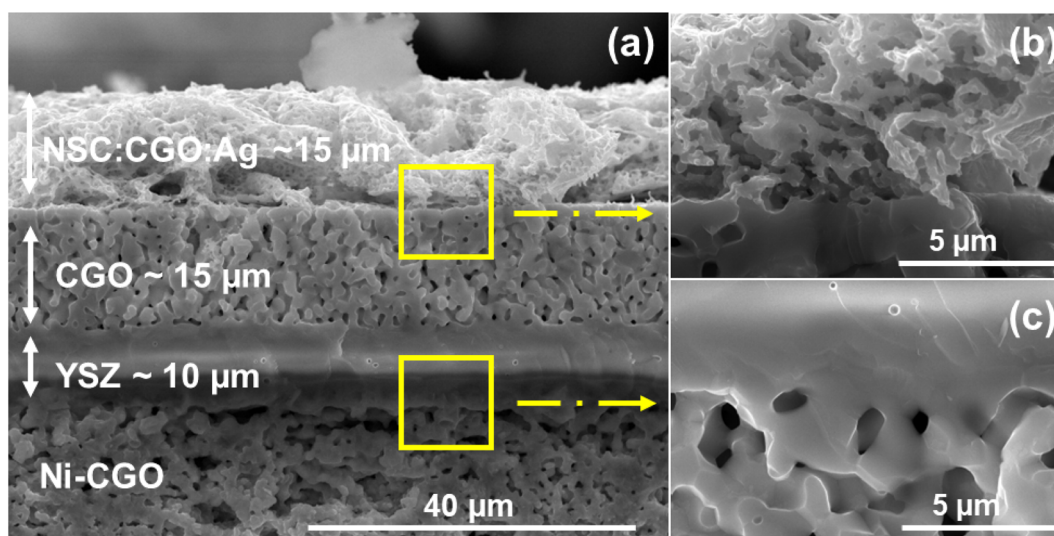


Fig. 14 SEM image of the single cell.



Furthermore, both interfaces between CGO-air composite electrode (Fig. 14(b)) and anode-YSZ electrolyte (Fig. 14(c)) present very good adherence without signs of cracks or delamination. Fig. S4† shows a cross-section of a single cell after testing in SOFC mode, in which no evidence of microstructural deterioration resulting from grain coarsening or cracking of the layers is observed. Fig. S5† shows the XRD pattern at room temperature of the cathode side of a single SOFC with configuration Ni-CGO/YSZ/CGO/(Nd,Gd)<sub>1/3</sub>Sr<sub>2/3</sub>CoO<sub>3-δ</sub>:Ce<sub>0.9</sub>(Gd,Nd)<sub>0.1</sub>O<sub>1.95</sub>:Ag after testing, in which the Ag NPs are clearly visible. The X-ray beam penetrates just to the CGO buffer layer, whereas the YSZ and anode layers are not detected.

The results of the electrochemical performance confirm that the Ag-decorated composite air electrode is a most promising IT-SOFC cathode material. In the present case, the simultaneous deposition of the composite cathode and decoration with Ag nanoparticles has been demonstrated and opens up new avenues for advanced processing of high-performance air electrodes for solid oxide cells using cost-effective and scalable spray-pyrolysis technology.

## 4. Conclusions

Spray pyrolysis is demonstrated as an efficient and scalable processing method for the synthesis, deposition and low-temperature sintering of composite electrodes of (Nd,Gd)<sub>1/3</sub>Sr<sub>2/3</sub>CoO<sub>3-δ</sub>:(Gd,Nd)<sub>0.1</sub>Ce<sub>0.9</sub>O<sub>1.95</sub> decorated with Ag nanoparticles. The improved microstructure of the spray-pyrolysed electrodes offers a smaller particle size with extended triple-phase boundary area, higher porosity and lower thickness compared to an analogous electrode composition deposited by slurry coating. The lowering sintering temperature of the spray-pyrolysed electrodes increases the active reaction surface, decreasing the high- and low-frequency impedance contributions to electrode polarisation. Moreover, decoration of the electrode surface with Ag nanoparticles lowers the low-frequency polarisation contribution at low temperatures (500–600 °C). The cathode composites decorated with Ag nanoparticles and prepared by spray-pyrolysis display an outstanding polarisation resistance at intermediate temperature (600 °C) of 0.18 Ω cm<sup>2</sup>, decreasing to 0.03 Ω cm<sup>2</sup> at 700 °C. EXAFS and XANES indicate that the catalytic effect of the nanoparticles results from their core-shell structure involving a thin Ag<sub>2</sub>O layer, which decomposes to metallic silver above 600 °C.

A fuel-cell test of a single cell based on spray-pyrolysed (Nd,Gd)<sub>1/3</sub>Sr<sub>2/3</sub>CoO<sub>3-δ</sub>:(Gd,Nd)<sub>0.1</sub>Ce<sub>0.9</sub>O<sub>1.95</sub>:Ag cathode deposited on a thin YSZ/CGO electrolyte and a Ni-CGO anode support exhibited power densities 0.07, 0.3 and 0.6 W cm<sup>-2</sup> at 500, 600 and 700 °C, respectively; the cathode polarisation had only a minor contribution to the total cell resistance.

## Author contributions

Paula Rosendo Santos: investigation, visualization; Domingo Pérez-Coll: conceptualization, methodology, supervision, validation, writing – review & editing; M. Teresa Azcondo:

investigation, visualization, writing – review & editing. Glenn C. Mather: conceptualization, methodology, supervision, validation, writing – review & editing; Álvaro Muñoz-Noval: investigation, data curation, visualization, writing – original draft; Eduardo Salas-Colera: investigation, data curation, visualization, writing – original draft; Ulises Amador: conceptualization, methodology, supervision, validation, writing – review & editing; Khalid Boulahya: investigation, visualization, writing – original draft; Daniel Muñoz-Gil: conceptualization, investigation, visualization, supervision, writing – original draft, writing – review & editing.

## Conflicts of interest

There are no conflicts to declare.

## Acknowledgements

We thank the project PID2019-106662RB-C41 funded by MCIN/AEI/10.13039/501100011033 and the project PID2021-123308OB-I00 funded by MCIN/AEI/10.13039/501100011033 and by “ERDF A way of making Europe”. PRS, MTA and UA are grateful to the USP-CEU for other financial support. We also thank BM5 Spline line and CSIC for allocating beamtime and facilitating access to the ESRF for XAS experiments.

## References

- Z. Gao, L. V. Mogni, E. C. Miller, J. G. Railsback and S. A. Barnett, *Energy Environ. Sci.*, 2016, **9**, 1602–1644.
- S. B. Adler, *Chem. Rev.*, 2004, **104**, 4791–4844.
- J. Fleig, *Annu. Rev. Mater. Res.*, 2003, **33**, 361–382.
- W. H. Kan, A. J. Samson and V. Thangadurai, *J. Mater. Chem. A*, 2016, **4**, 17913–17932.
- E. V. Tsipis and V. V. Kharton, *J. Solid State Electrochem.*, 2008, **12**, 1039–1060.
- A. Kumar, P. S. Devi, A. D. Sharma and H. S. Maiti, *J. Am. Ceram. Soc.*, 2005, **88**, 971–973.
- D. Beckel, U. P. Muecke, T. Gyger, G. Florey, A. Infortuna and L. J. Gauckler, *Solid State Ionics*, 2007, **178**, 407–415.
- L. dos Santos-Gómez, J. M. Porrás-Vázquez, E. R. Losilla, F. Martín, J. R. Ramos-Barrado and D. Marrero-López, *J. Eur. Ceram. Soc.*, 2018, **38**, 1647–1653.
- V. Zapata-Ramírez, P. Rosendo-Santos, U. Amador, C. Ritter, G. C. Mather and D. Pérez-Coll, *Renewable Energy*, 2022, **185**, 1167–1176.
- V. Zapata-Ramírez, L. dos Santos-Gómez, G. C. Mather, D. Marrero-López and D. Pérez-Coll, *ACS Appl. Mater. Interfaces*, 2020, **12**, 10571–10578.
- B. Kamecki, J. Karczewski, P. Jasiński and S. Molin, *Adv. Mater. Interfaces*, 2021, **8**, 2002227.
- R. Sažinas, K. B. Andersen and K. K. Hansen, *J. Solid State Electrochem.*, 2020, **24**, 609–621.
- R. Sažinas, K. B. Andersen, S. B. Simonsen, P. Holtappels and K. K. Hansen, *J. Electrochem. Soc.*, 2019, **166**, F79.
- Y. Zhu, W. Zhou, R. Ran, Y. Chen, Z. Shao and M. Liu, *Nano Lett.*, 2016, **16**, 512–518.



- 15 G. He, X. Liu, R. Li, D. Zhai, Y. Liu, C. Xie, P. Hu, Q. Zhen, S. Bashir and J. Liu, *ACS Appl. Mater. Interfaces*, 2020, **12**, 9421–9433.
- 16 Y. Liu, M. Mori, Y. Funahashi, Y. Fujishiro and A. Hirano, *Electrochem. Commun.*, 2007, **9**, 1918–1923.
- 17 R. Su, Z. Lü, S. P. Jiang, Y. Shen, W. Su and K. Chen, *Int. J. Hydrogen Energy*, 2013, **38**, 2413–2420.
- 18 D. Muñoz-Gil, M. T. Azcondo, C. Ritter, O. Fabelo, D. Pérez-Coll, G. C. Mather, U. Amador and K. Boulahya, *Inorg. Chem.*, 2020, **59**, 12111–12121.
- 19 A. Varma, A. S. Mukasyan, A. S. Rogachev and K. V. Manukyan, *Chem. Rev.*, 2016, **116**, 14493–14586.
- 20 J. Rodríguez-Carvajal, *Phys. B*, 1993, **192**, 55–69.
- 21 B. Ravel and M. Newville, *J. Synchrotron Radiat.*, 2005, **12**, 537–541.
- 22 I.-K. Suh, H. Ohta and Y. Waseda, *J. Mater. Sci.*, 1988, **23**, 757–760.
- 23 P. Norby, R. Dinnebier and A. N. Fitch, *Inorg. Chem.*, 2002, **41**, 3628–3637.
- 24 Johnson, D. ZView, *A Software Program for IES Analysis*, Scribner Associates, Inc., 2005.
- 25 J. T. S. Irvine, D. C. Sinclair and A. R. West, *Adv. Mater.*, 1990, **2**, 132–138.
- 26 S. B. Adler, *Solid State Ionics*, 1998, **111**, 125–134.
- 27 D. Feng, Y. Feng, S. Yuan, X. Zhang and G. Wang, *Appl. Therm. Eng.*, 2017, **111**, 1457–1463.
- 28 M. Shao, Q. Chang, J.-P. Dodelet and R. Chenitz, *Chem. Rev.*, 2016, **116**, 3594–3657.
- 29 X. Bao, M. Muhler, T. Schedel-Niedrig and R. Schlögl, *Phys. B*, 1996, **54**, 2249–2262.
- 30 J. Y. Sun, Z. K. Wang, H. S. Lim, S. C. Ng, M. H. Kuok, T. T. Tran and X. Lu, *ACS Nano*, 2010, **4**, 7692–7698.
- 31 J. Chen, R. Zhang, L. Han, B. Tu and D. Zhao, *Nano Res.*, 2013, **6**, 871–879.
- 32 J. C. Park, H. J. Lee, J. Y. Kim, K. H. Park and H. Song, *J. Phys. Chem. C*, 2010, **114**, 6381–6388.
- 33 A. Roßberg, T. Reich and G. Bernhard, *Anal. Bioanal. Chem.*, 2003, **376**, 631–638.
- 34 Á. Muñoz-Noval, K. Fukami, A. Koyama, D. Gallach, D. Hermida-Merino, G. Portale, A. Kitada, K. Murase, T. Abe, S. Hayakawa and T. Sakka, *Electrochem. Commun.*, 2016, **71**, 9–12.
- 35 Y. Sun, L. Zhuang, J. Lu, X. Hong and P. Liu, *J. Am. Chem. Soc.*, 2007, **129**, 15465–15467.
- 36 P. Crespo, R. Litrán, T. C. Rojas, M. Multigner, J. M. de la Fuente, J. C. Sánchez-López, M. A. García, A. Hernando, S. Penadés and A. Fernández, *Phys. Rev. Lett.*, 2004, **93**, 087204.
- 37 P. Zhang and T. K. Sham, *Appl. Phys. Lett.*, 2002, **81**, 736–738.
- 38 I. L. Garzón, C. Rovira, K. Michaelian, M. R. Beltrán, P. Ordejón, J. Junquera, D. Sánchez-Portal, E. Artacho and J. M. Soler, *Phys. Rev. Lett.*, 2000, **85**, 5250–5251.
- 39 J. F. Weaver and G. B. Hoflund, *Chem. Mater.*, 1994, **6**, 1693–1699.
- 40 J.-H. Wang, M. Liu and M. C. Lin, *Solid State Ionics*, 2006, **177**, 939–947.
- 41 R. Küngas, A. S. Yu, J. Levine, J. M. Vohs and R. J. Gorte, *J. Electrochem. Soc.*, 2013, **160**, F205.
- 42 R. Merkle, J. Maier and H. J. M. Bouwmeester, *Angew. Chem., Int. Ed.*, 2004, **43**, 5069–5073.
- 43 E. Pikalova, N. Bogdanovich, A. Kolchugin, K. Shubin, L. Ermakova, N. Ereemeev, A. Farlenkov, A. Khrustov, E. Filonova and V. Sadykov, *Int. J. Hydrogen Energy*, 2021, **46**, 16947–16964.

